

# Heteronuclear and Homonuclear Radio Frequency Driven Recoupling

**Authors:** Evgeny Nimerovsky\*, Kai Xue, Kumar Tekwani Movellan & Loren B. Andreas\*

## **Affiliations:**

Department of NMR based Structural Biology, Max Planck Institute for Biophysical Chemistry, Am Fassberg 11, Göttingen, Germany

\*Corresponding authors: land@nmr.mpibpc.mpg.de ORCID: 0000-0003-3216-9065 and evni@nmr.mpibpc.mpg.de

## **Abstract**

The Radio Frequency Driven Recoupling (RFDR) pulse sequence is used in magic-angle spinning (MAS) NMR to recouple homonuclear dipolar interactions. Here we show simultaneous recoupling of both the heteronuclear and homonuclear dipolar interactions by applying RFDR pulses on two channels. We demonstrate the method, called HETeronuclear RFDR (HET-RFDR) on microcrystalline SH3 samples at 10 kHz and 55.555 kHz MAS. Numerical simulations of both HET-RFDR and standard RFDR sequences allow better understanding of the influence of offsets, paths of magnetization transfers for both HET-RFDR and RFDR experiments as well as the crucial role of XY phase cycling.

Keywords: Magic Angle Spinning NMR, heteronuclear and homonuclear RFDR, the operator analysis

## **Introduction**

Magic-angle spinning (MAS) NMR spectroscopy is used to obtain atomic resolution spectra of materials and biological molecules in the solid state, by removal of the broadening associated with anisotropic dipolar couplings and other interactions. Under control of radio frequency pulses, dipolar

22 interactions can be switched on, or recoupled, in order to correlate nearby spins or to accurately determine  
23 internuclear distances. Recoupling sequences can be broadly categorized as homonuclear (Meier and Earl,  
24 1986; Tycko and Dabaghi, 1990; Gullion and Vega, 1992; Bennett et al., 1992; Ok et al., 1992; Zhang et  
25 al., 2020; Gelenter et al., 2020; Takegoshi et al., 2001; Szeverenyi et al., 1982; Hou et al., 2011b, 2013;  
26 Carravetta et al., 2000; Bennett et al., 1998; Nielsen et al., 2012) or heteronuclear (Gelenter et al., 2020;  
27 Gullion and Schaefer, 1989; Jaroniec et al., 2002; Hing et al., 1992; Hartmann and Hahn, 1962; Rovnyak,  
28 2008; Metz et al., 1994; Hediger et al., 1994; Hou et al., 2011a; Brinkmann and Levitt, 2001; Gelenter and  
29 Hong, 2018; Zhang et al., 2016; Nielsen et al., 2012).

30 The recoupling of the homonuclear dipolar interactions with a train of  $\pi$ -pulses every rotor period  
31 was originally introduced by Gullion and Vega (Gullion and Vega, 1992) and Bennett et al (Bennett et al.,  
32 1992). Since, the homonuclear Radio Frequency Driven Recoupling (RFDR) sequence (Bennett et al.,  
33 1992) has been successfully applied for the qualitative and quantitative determinations of the dipolar spin  
34 correlations in materials (Saalwächter, 2013; Messinger et al., 2015; Fritz et al., 2019; Roos et al., 2018;  
35 Nishiyama et al., 2014a; Wong et al., 2020; Hellwagner et al., 2018; Pandey and Nishiyama, 2018) and  
36 biomolecular samples (Zheng et al., 2007; Tang et al., 2011; Shen et al., 2012; Pandey et al., 2014; Grohe  
37 et al., 2019; Andreas et al., 2015; Petkova et al., 2002; Aucoin et al., 2009; Zinke et al., 2018; Zhang et al.,  
38 2017; Zhou et al., 2012; Jain et al., 2017; Colvin et al., 2015; Shi et al., 2015; Daskalov et al., 2020). Sun  
39 et al. (1995) showed that the RFDR pulse sequence element could also be used as a part of the SPICP  
40 experiment (Wu and Zilm, 1993) for removing the undesired effect of the chemical shift terms to zero order.

41 Depending on the assumptions (Bennett et al., 1992; Gullion and Vega, 1992; Ishii, 2001), two  
42 different Average Hamiltonian Theory (Haeberlen and Waugh, 1968; Maricq, 1982) (AHT) descriptions  
43 have been detailed for RFDR. In both, homonuclear dipolar recoupling occurs via a rotor-synchronized  
44 train of  $\pi$ -pulses, with one pulse each rotor period (Bennett et al., 1992) on a single channel. In the first  
45 case, delta  $\pi$ -pulses are assumed (Bennett et al., 1992). The efficiency of recoupling is linked with the  
46 rotational resonance conditions (Bennett et al., 1992, 1998), and depends on the ratio between chemical

47 shift offset difference and MAS rate. In the second theoretical description, the effects of finite  $\pi$ -pulses are  
 48 considered (Bennett et al., 1992; Ishii, 2001; Nishiyama et al., 2014b; Zhang et al., 2015; Brinkmann et al.,  
 49 2002; Ji et al., 2020). The efficiency of recoupling in this case depends on a duty factor (Ishii, 2001), defined  
 50 as the fraction of the rotor period occupied by the  $\pi$ -pulse. The RFDR pulses are applied according to a  
 51 variety of XY phase cycling schemes, which have been analyzed with the intent to suppress imperfections  
 52 associated with offset differences, rf-field inhomogeneity and second order Average Hamiltonian terms  
 53 between different anisotropic interactions (Zhang et al., 2015).

54 The full high field truncated dipolar Hamiltonian of the homonuclear  $I_2$  spin system is represented  
 55 as follows:

$$56 \quad H_{D,Full}^H = \omega_{D,12}(t)[3I_{z1}I_{z2} - \bar{I}_1 \cdot \bar{I}_2]. \quad \text{Eq. (1)}$$

57 where  $\omega_{D,12}(t)$  is a periodic time dependent function (Olejniczak et al., 1984) that depends on the  
 58 positions of spins  $I_1$  and  $I_2$  within the rotor. This Hamiltonian is subsequently referred to as the full  
 59 Hamiltonian, and contains only the A and B terms of the dipolar alphabet (Slichter, 1990).

60 The interesting conclusion can be obtained, if we simplify the Eq. (1). The dipolar Hamiltonian  
 61 during RFDR can be simplified (in the absence of other interactions) by considering that  $\bar{I}_1 \cdot \bar{I}_2$  commutes  
 62 with the secular part ( $I_{z1}I_{z2}$ ) and with the rf-field Hamiltonian. At the end of each rotor period, the  
 63 oscillatory  $\omega_{D,12}(t)$  term ensures zero total evolution. The simplified Eq. (1) is:

$$64 \quad H_{D,M}^H = 1.5\omega_{D,12}(t)2I_{z1}I_{z2}. \quad \text{Eq. (2)}$$

65 Comparing Eq. (2) with full Dipolar Hamiltonian of the heteronuclear  $IS$  spin system(Mehring, 1983):

$$66 \quad H_{D,Full}^{IS} = \omega_{D,12}(t)2I_zS_z, \quad \text{Eq. (3)}$$

67 we notice that the difference between Eq. (3) and Eq. (1) is a factor of 1.5. Note that we have made the  
 68 substitution of  $I_{z1}$  to  $I_z$  and  $I_{z2}$  to  $S_z$  while the dipolar function,  $\omega_{D,12}(t)$ , has been kept the same. Such

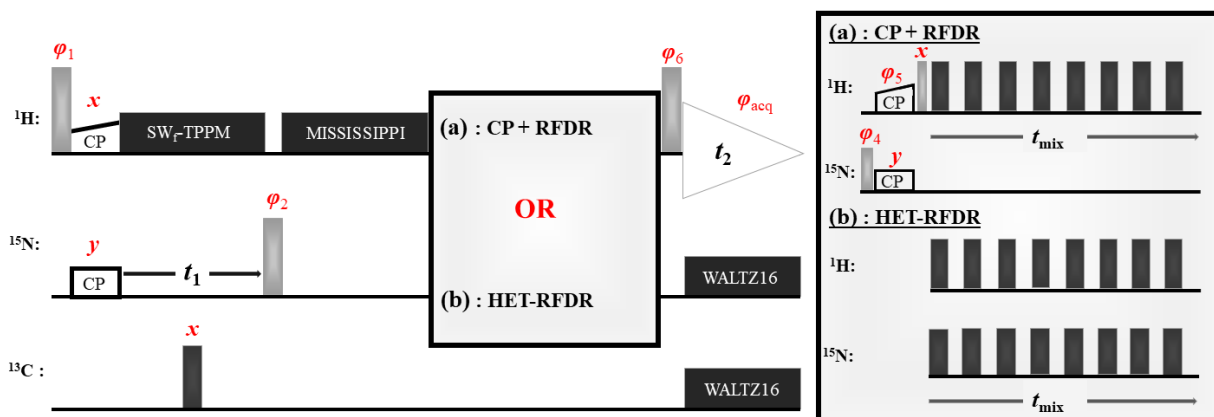
69 comparison suggests a HETeronuclear-RFDR (HET-RFDR), which should have a scaling of 1.5 as  
70 compared with the homonuclear case.

71 In this article we investigate spin dynamics under HET-RFDR, in which RFDR  $\pi$ -pulses are  
72 applied simultaneously on two channels (Figure 1). We demonstrate simultaneous heteronuclear and  
73 homonuclear transfers using HET-RFDR applied to  $\alpha$ -PET (Movellan et al., 2019) labeled SH3 at 10 kHz  
74 and 55.555 kHz MAS.

75 We perform and compare a numerical operator analysis of both RFDR and HET-RFDR  
76 experiments under different simulated conditions. This numerical analysis allows to define the conditions  
77 under which homonuclear and heteronuclear RFDR polarization transfers have similar behaviors, to  
78 understand the paths through which the signals are transferred between operators, and to understand the  
79 crucial role of 90 degree phase alternation (XY-4, XY-8, etc) (Ishii, 2001; Nishiyama et al., 2014b; Zhang  
80 et al., 2015; Hellwagner et al., 2018) for both RFDR and HET-RFDR recoupling.

## 81 **HET-RFDR Experiments**

82 Figure 1 shows two 2D (H)N(H)H pulse sequences used to evaluate the HET-RFDR transfer. For  
83 both sequences, the transfer from proton to nitrogen is implemented with ramped cross polarization (CP)  
84 and then the nitrogen dimension is encoded ( $t_1$ ) for 2D spectra. In Figure 1a, the transfer to structurally  
85 interesting protons is implemented with N to H CP followed by H-H RFDR. In Figure 1b, the same  
86 transfer is implemented with a single HET-RDFR period. The HET-RFDR transfer avoids the back CP  
87 step. Instead, nitrogen polarization is placed along the  $\hat{z}$  axis and transferred to directly bonded proton  
88 spins and at the same time to remote proton spins with the simultaneous application of the  $\pi$ -pulses on the  
89 proton and nitrogen channels.



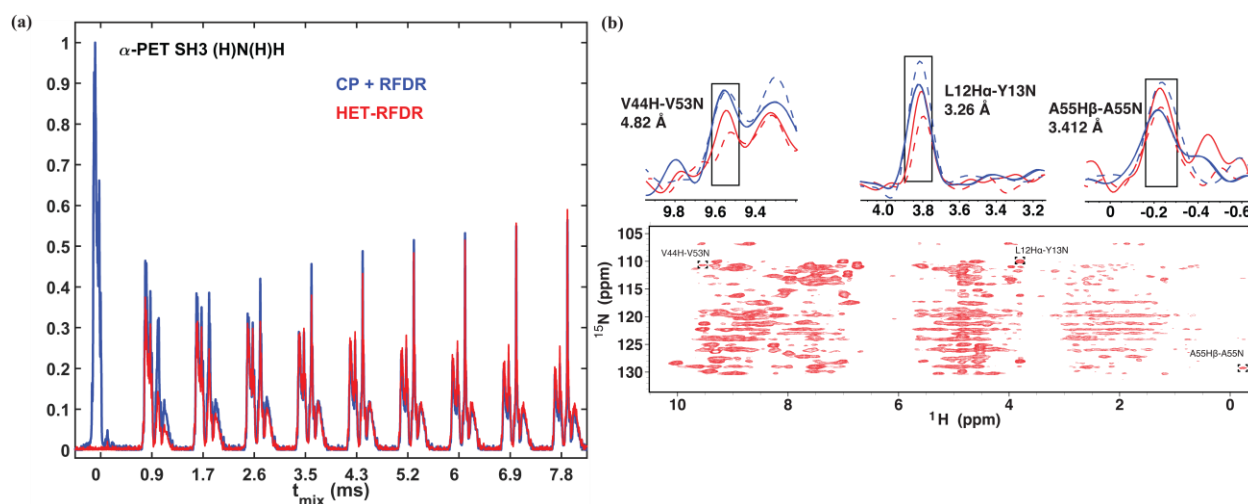
90

91 **Figure 1** Two versions of the (H)N(H)H pulse sequence are shown. The first, (a), is the standard implementation with CP +  
 92 RFDR. The second, (b), instead uses the new HET-RFDR recoupling element. Light grey pulses represent  $\pi/2$ -pulses, whereas  
 93 dark grey pulses represent  $\pi$ -pulses. The ramped CP transfer from proton to nitrogen as well as from nitrogen to proton in (a) are  
 94 indicated with constant power on the nitrogen channel and a ramp in power on the proton channel. During the indirect dimension  
 95 ( $t_1$ ), SW<sub>r</sub>-TPPM decoupling is applied at 55 kHz, respectively. A single  $\pi$ -pulse in the middle of  $t_1$  decouples carbon. Water  
 96 suppression is implemented with the MISSISSIPPI (Zhou and Rienstra, 2008) sequence. During acquisition, WALTZ16 (Thakur et  
 97 al., 2006) decoupling is applied on nitrogen and carbon channels. The phases are:  $\varphi_1 = x, -x$ ;  $\varphi_{acq} = y, -y, -y, y, -y, y, y, -y$ .  
 98 In (a) the phases are:  $\varphi_2 = x$ ;  $\varphi_4 = x, x, -x, -x$ ;  $\varphi_5 = y, y, y, y, -y, -y, -y, -y$ ;  $\varphi_6 = x$ . In (b) the phases are:  $\varphi_2 =$   
 99  $x, x, -x, -x$ ;  $\varphi_6 = x, x, x, x, -x, -x, -x, -x$ . RFDR  $\pi$ -pulses on both channels use the XY8 scheme (Gullion et al., 1990).

100 Figure 2 compares the 1D and 2D spectra obtained with the two sequences of Figure 1. In Figure  
 101 2a, the 1D signal is shown as a function of RFDR mixing time. For the standard sequence (blue) the N to  
 102 H CP was 0.55 ms. The HET-RFDR signal is shown in (red). Without RFDR mixing, the CP+RFDR  
 103 detects directly bonded amide protons (Figure 2a, red with zero mixing time) and zero signal occurs for  
 104 HET-RFDR (Figure 2a, blue with zero mixing time) since the signal is on nitrogen. With increasing  
 105 RFDR mixing, the signal is transferred from directly bonded amide protons to remote protons for the  
 106 CP+RFDR sequence (red), whereas simultaneous transfer from nitrogen spins to amide protons and from  
 107 amide protons to remote protons occurs with HET-RFDR (blue). For the directly bonded amide protons,  
 108 the HET-RFDR polarization transfer achieves only ~40% of the CP signal. This occurs at 0.846 ms  
 109 mixing (second red spectrum). However, with increased mixing of about 3 ms, HET-RFDR reaches the

110 same efficiency as the standard sequence. This is notable since transfer over long distances has been  
111 implemented with ~3 ms mixing for deuterated samples (Grohe et al., 2019; Linser et al., 2014).

112 Structurally interesting cross-peaks are indeed observed in the 2D HET-RFDR spectrum shown in  
113 Figure 2b at 3.456 ms mixing. For example, we have observe the amide-amide contact between V44 and  
114 V53, which is 4.82 Å in the crystal (pdb code 2NUZ (Castellani et al., 2002)). The amide to side chain  
115 contact of a A55 N to H $\beta$  (3.41 Å) is also indicated in the Figure, along with a sequential contact from  
116 Y13  $^{15}\text{N}$  to L12  $^1\text{H}\alpha$ , which is 3.26 Å. These peaks are boxed in Figure 2b, and the 1D slices shown above  
117 the 2D spectra. For comparison, in 1D slices we show CP +RFDR (blue) and HET-RFDR (red) intensities  
118 of these three peaks for two different mixing times: 1.154 ms (dashed) 3.456 ms (solid). Both methods  
119 provide similar intensities at long mixing time, whereas at shorter mixing times CP+RFDR provides  
120 higher intensities for short range distances.



122 **Figure 2** 1D (a) and 2D (b) (H)N(H)H spectra of  $\alpha$ -PET labeled SH3. For all spectra the first CP from proton to nitrogen was  
123 performed with 1.05 ms. (a) 1D spectra with different sequences used for the second transfer: CP + RFDR (blue) and HET-RFDR  
124 (red). For CP + RFDR, 0.55 ms of CP was used. For both RFDR and HET-RFDR,  $t_{\text{mix}}$  of 0, 0.846, 1.728, 2.592, 3.456, 4.32,  
125 5.184, 6.048, 6.912, 7.7776 ms are shown. (b) 2D HET-RFDR at 3.456 ms of mixing time. Spectra were recorded at a 600 MHz  
126 Bruker instrument equipped with a 1.3 mm probe and an MAS frequency of 55 kHz. The widths of  $\pi$ -pulses on proton and  
127 nitrogen channels were 5.8  $\mu\text{s}$  and 6.6  $\mu\text{s}$ , respectively. The 1D slices show the intensities of three selected peaks. CP+RFDR

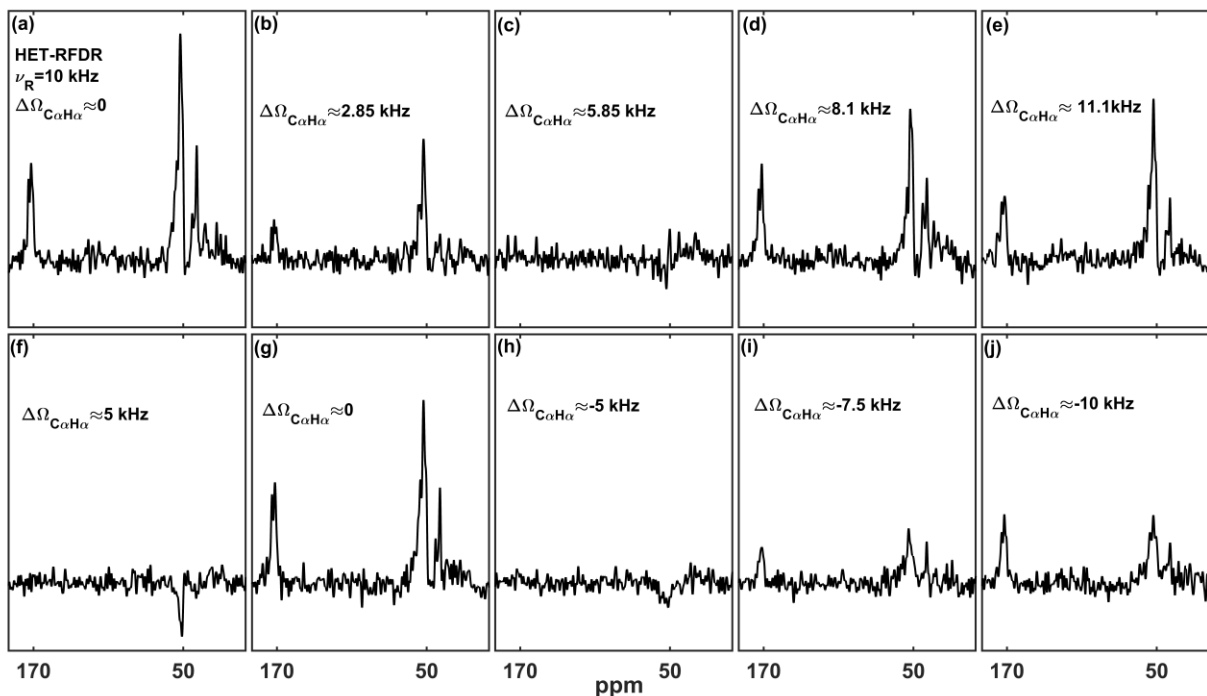
128 (blue) and HET-RFDR (red)- at 1.154 ms (dashed lines) and 3.456 ms (solid lines) mixing are displayed. The experimental  
129 parameters are detailed in Table 1 and 2 the 'Experimental Methods'. XY8 phase cycling was used.

130 At 55.555 kHz MAS on a 600 MHz instrument, the chemical shift offsets can always be much  
131 smaller than the spinning frequency. At a lower MAS frequency, the offsets become important for HET-  
132 RFDR. The recoupling then depends on a heteronuclear 'offset difference' that we define as  $\Delta\Omega_{ij} = \Omega_i -$   
133  $\Omega_j$ , where  $\Omega_i$  and  $\Omega_j$  are the offsets on each channel (the difference between the Larmor frequency of the  
134 spin and the carrier frequency (Bak et al., 2000)). When  $\Omega_i = \Omega_j = 0$  as well as  $\Delta\Omega_{ij} = \Omega_i - \Omega_j \approx n\nu_R$   
135 ( $n=0, \pm 1, \pm 2 \dots$ ), the HET-RFDR polarization transfer reaches local maximal intensities. However, when  
136  $\Delta\Omega_{ij} = \Omega_i - \Omega_j \approx 0.5n\nu_R$  ( $n=\pm 1, \pm 3 \dots$ ), the HET-RFDR polarization transfer reaches local minima. The  
137 experimental confirmation of this is shown in Figure 3, where the effect of different proton and carbon  
138 offsets is explored for proton-carbon HET-RFDR spectra. The spinning frequency was reduced to 10 kHz  
139 MAS for these measurements and the signal detected on the carbon channel. The 1D HC HET-RFDR  
140 pulse sequence is shown in the SI (Figure S1).

141 Figures 3a-e depicts the HET-RFDR spectra when the carbon carrier frequency is changed (numbers  
142 show the offset from the alpha carbon at ~53 ppm), whereas the alpha proton offset is kept at 0 kHz (at  
143 4.6 ppm). While heteronuclear transfer is detected at zero offset (Figure 3a) or with 11.1 kHz carbon  
144 offset (Figure 3e), the signal remains in the noise when the carbon offset is 5.85 kHz (Figure 3c).

145 A similar effect can be detected when the proton carrier frequency is changed (increased from 4.6 ppm),  
146 but this time the carbon offset is set to 5 kHz from C $\alpha$  (83.66 ppm) to show that it is the offsets on both  
147 channels ( $\Delta\Omega_{C\alpha H\alpha}$ ) that is important (Figures 3f-j). The series of spectra show a local minimal transfers at  
148 offset differences of 5 kHz (Figure 3f) and -5 kHz (Figure 3h) and local maximal polarization transfers at

149 differences of 0 (Figure 3g) and -10 kHz (Figure 3j).



150

151 **Figure 3** The influence of the carbon and proton offsets on proton-carbon HET-RFDR polarization transfers at 4.8 ms mixing.  
152  $\alpha$ -PET labeled SH3 was used with 10 kHz MAS at a 600 MHz spectrometer using a 1.3 mm probe. The widths of  $\pi$ -pulses on  
153 proton and carbon channels were 5.8 us and 6.6 us, respectively. For (a)-(e) the proton carrier frequency was set to 4.6 ppm and  
154 carbon carrier frequency was set to 51 ppm (a), 70 ppm (b), 90 ppm (c), 105 ppm (d) 125 ppm (e). For (f)-(j) the carbon carrier  
155 frequency was set to 83.66 ppm and the proton carrier frequency was set to 4.6 ppm (f), 12.933 ppm (g), 21.26 ppm (h), 25.43  
156 ppm (i) and 29.6 ppm (j). The indicated offset differences,  $\Delta\Omega_{C\alpha H\alpha} = \Omega_{C\alpha} - \Omega_{H\alpha}$  in kHz were calculated based on typical  
157 isotropic chemical shifts of  $C_{\alpha}$  (51 ppm) and  $H_{\alpha}$  (4.6 ppm) at a 600 MHz spectrometer. The experimental parameters are detailed  
158 in Table 1 and 2 the ‘Experimental Methods’. The 1D HET-RFDR sequence is shown in the SI (Figure S1). [XY8 phase cycling](#)  
159 [was used.](#)

## 160 Numerical Operator Analysis

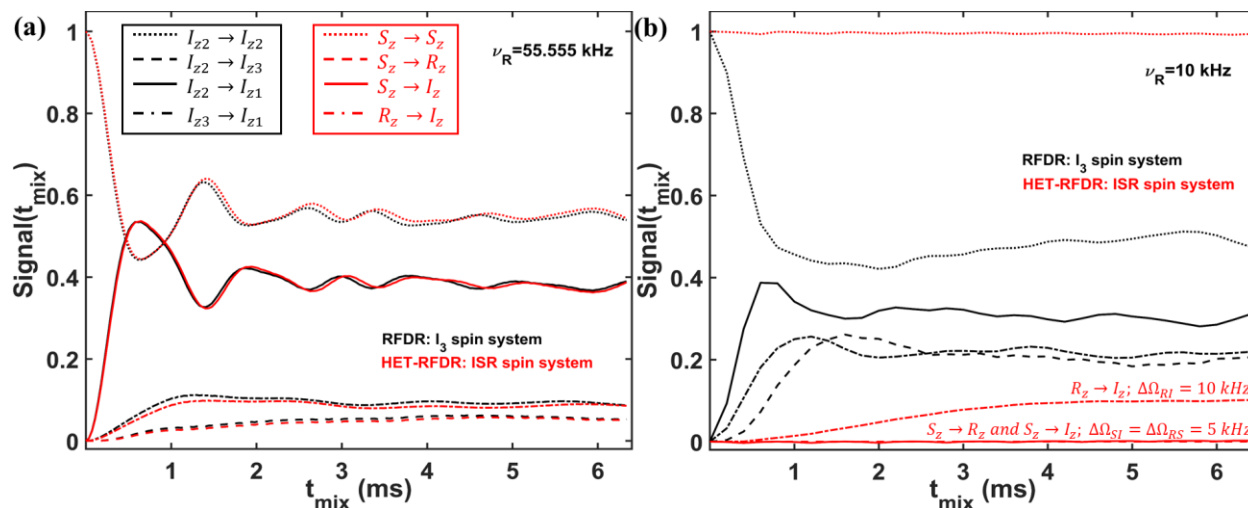
161 To comprehend the mechanism underlying the transfers during the HET-RFDR and also the well-  
162 known RFDR pulse sequence, we use a numerical simulation approach. We identify the conditions under  
163 which the heteronuclear and homonuclear spin systems under HET-RFDR and RFDR sequences have  
164 similar behaviors. Considering the evolutions of the different spin systems through HET-RFDR and



165 RFDR during the first two rotor periods, we identify the operators that are involved in the polarization  
166 transfer.

167 To identify the conditions under which the HET-RFDR and RFDR sequences have similar and  
168 different behaviors we simulated a three spin system at high (55.555 kHz) and low (10 kHz) MAS  
169 frequencies. In Figure 4 we compare the RFDR transferred signals for  $I_3$  (a homonuclear 3-spin system,  
170 black lines) and HET-RFDR transferred signals for  $ISR$  (three different types of spins with the names  $I$ ,  $S$   
171 and  $R$ ; red lines) spin systems. At 55.555 Hz MAS when the offset difference is small compared to MAS  
172 rate, the behavior of the homonuclear  $I_3$  spin system is similar to the behavior of the heteronuclear  $ISR$   
173 spin system (Figure 4a). However, when the MAS rate is low (10 kHz) and the offset difference cannot be  
174 neglected, the behaviors of these spin systems are completely different (Figure 4b). For the homonuclear  
175 spin system ( $I_3$ ), the polarization transfers are efficient for all dipolar pairs (black lines), whereas for the  
176 heteronuclear spin system ( $ISR$ ) the HET-RFDR polarization transfer is detected between  $R$  and  $I$  spins  
177 (Figure 4b, red dashed-dotted line) only. For this  $RI$  pair the offset difference was chosen as 10 kHz,  
178 whereas for the other spin pairs ( $SI$ ,  $RS$ ) the offset differences were set to 5 kHz. These simulations show  
179 a special condition of  $\sim 0.5\nu_R$  of offset difference for the heteronuclear spins under which the transfer  
180 obtains local / global minima values. The simulations are in full agreement with the experiments, which  
181 were shown in Figure 3. Another interesting observation can be made from the influence of the offset  
182 difference on the RFDR transfer for the homonuclear  $I_3$  spin system (Figure 4b, black lines). For a 5 kHz  
183 of offset difference, the RFDR polarization transfer between  $I_{z2}$  and  $I_{z3}$  spins is significantly faster with 10  
184 kHz MAS (Figure 4b, black dashed line) than at 55.555 kHz MAS (Figure 4a, black dashed line). Since  
185 the duty factor is decreased with decreasing MAS frequency (Ishii, 2001): 0.33 for 55.555 kHz MAS and  
186 0.06 for 10 kHz MAS, the opposite behavior is expected if one considers only the effect of finite pulses in  
187 the RFDR experiment (Ishii, 2001). It indicates that when the offset difference cannot be neglected with  
188 respect to the MAS rate, it has a significant influence on the RFDR transfer efficiency between

189 homonuclear spins despite the significant remoteness from the rotational resonance condition (Bennett et  
 190 al., 1992, 1998).



191  
 192 **Figure 4** Comparison of the simulated RFDR and HET-RFDR signals. *I*<sub>3</sub> (three homonuclear spins, black lines) and *ISR* (three  
 193 different spin types, red lines) for 55.555 kHz (a) and 10 kHz (b) MAS. 83 kHz of rf-field is used (6 us of the widths of  $\pi$ -pulses).  
 194 The vertical axis shows the intensities of the starting and transferred signals between different operators of *I*<sub>3</sub> and *ISR* spin  
 195 systems, respectively (the initial operator → the measured operator): *I*<sub>z2</sub> → *I*<sub>z2</sub> and *S*<sub>z</sub> → *S*<sub>z</sub> – (the dotted lines); *I*<sub>z2</sub> → *I*<sub>z3</sub> and  
 196 *S*<sub>z</sub> → *R*<sub>z</sub> – (the dashed lines); *I*<sub>z2</sub> → *I*<sub>z1</sub> and *S*<sub>z</sub> → *I*<sub>z</sub> – (the solid lines); *I*<sub>z3</sub> → *I*<sub>z1</sub> and *R*<sub>z</sub> → *I*<sub>z</sub> – (the dashed-dotted lines). For  
 197 both spin systems the offset ( $\Omega$ ) and CSA values are: [-3; 2; 7] (kHz) and [5.2; 2.5; 3]. The dipolar coupling constants for  
 198 homonuclear spin system (*I*<sub>3</sub>) spin system are:  $\nu_{12,D} = 7.333$  kHz,  $\nu_{13,D} = 2$  kHz,  $\nu_{23,D} = 0.333$  kHz. For *ISR* spin system all  
 199 dipolar constants are 1.5 times larger:  $\nu_{1S,D} = 11$  kHz,  $\nu_{1R,D} = 3$  kHz,  $\nu_{SR,D} = 0.5$  kHz. The simulated measurements occurs  
 200 every 2 rotor periods. XY8 phase cycling is used. *I*<sub>z1</sub> → *I*<sub>z1</sub>, *I*<sub>z3</sub> → *I*<sub>z3</sub>, *I*<sub>z</sub> → *I*<sub>z</sub> and *R*<sub>z</sub> → *R*<sub>z</sub> are not shown.

201 In order to understand via which operators the polarization transfer occurs, we considered the  
 202 evolutions of two systems - *I*<sub>2</sub> homonuclear and *IS* heteronuclear spin systems - under RFDR and HET-  
 203 RFDR sequences with 10 kHz MAS. We simulated the polarization transfers between different operators  
 204 during the first two rotor periods, which completes the basic RFDR element:  $t(\pi_x) \rightarrow del_1 \rightarrow t(\pi_y) \rightarrow$   
 205  $del_2$ . We consider the amplitudes of the operators for a single molecular orientation since it allows to see  
 206 the significant evolution of the operators during the two rotor periods. Figure 5a,c,e shows the amplitudes  
 207 of four Cartesian operators (Ernst et al., 1987) for *IS* (HET-RFDR) and Figures 5b,d,f shows the operators

208 for  $I_2$  (RFDR) spin systems. The measured Cartesian operators are  $I_z, S_z, 2I_xS_y, 2I_yS_x$  and  
 209  $I_{z1}, I_{z2}, 2I_{x1}I_{y2}, 2I_{y1}I_{x2}$  for  $IS$  and  $I_2$  spin systems, respectively.

210 The evolutions of four operators *during* two rotor periods for the  $IS$  spin system the  $I_2$  spin system are  
 211 different, regardless of the offset difference. However, with a zero offset difference, the simulated  
 212 heteronuclear operators (Figure 5a) and the homonuclear operators (Figure 5b) show the same values of  
 213 the amplitudes at one and two rotor periods. From the 64 possibilities (details in the SI, section ‘The  
 214 Operator Paths’) for magnetization transfer between heteronuclear operators  $I_z$  and  $S_z$  during the two rotor  
 215 periods, we find only one path with nonzero amplitude:  $I_z \xrightarrow{\pi_x} 2I_xS_y \xrightarrow{del_1} 2I_xS_y \xrightarrow{\pi_y} S_z \xrightarrow{del_2} S_z$ . In contrast to  
 216 the single path found for HET-RFDR, for the homonuclear case all 64 paths connecting operators  $I_{z1}$  and  
 217  $I_{z2}$  have non-zero amplitudes. However, after each rotor period, the sum of all homonuclear paths provides  
 218 the same values of the amplitudes as for the heteronuclear  $IS$  spin system.

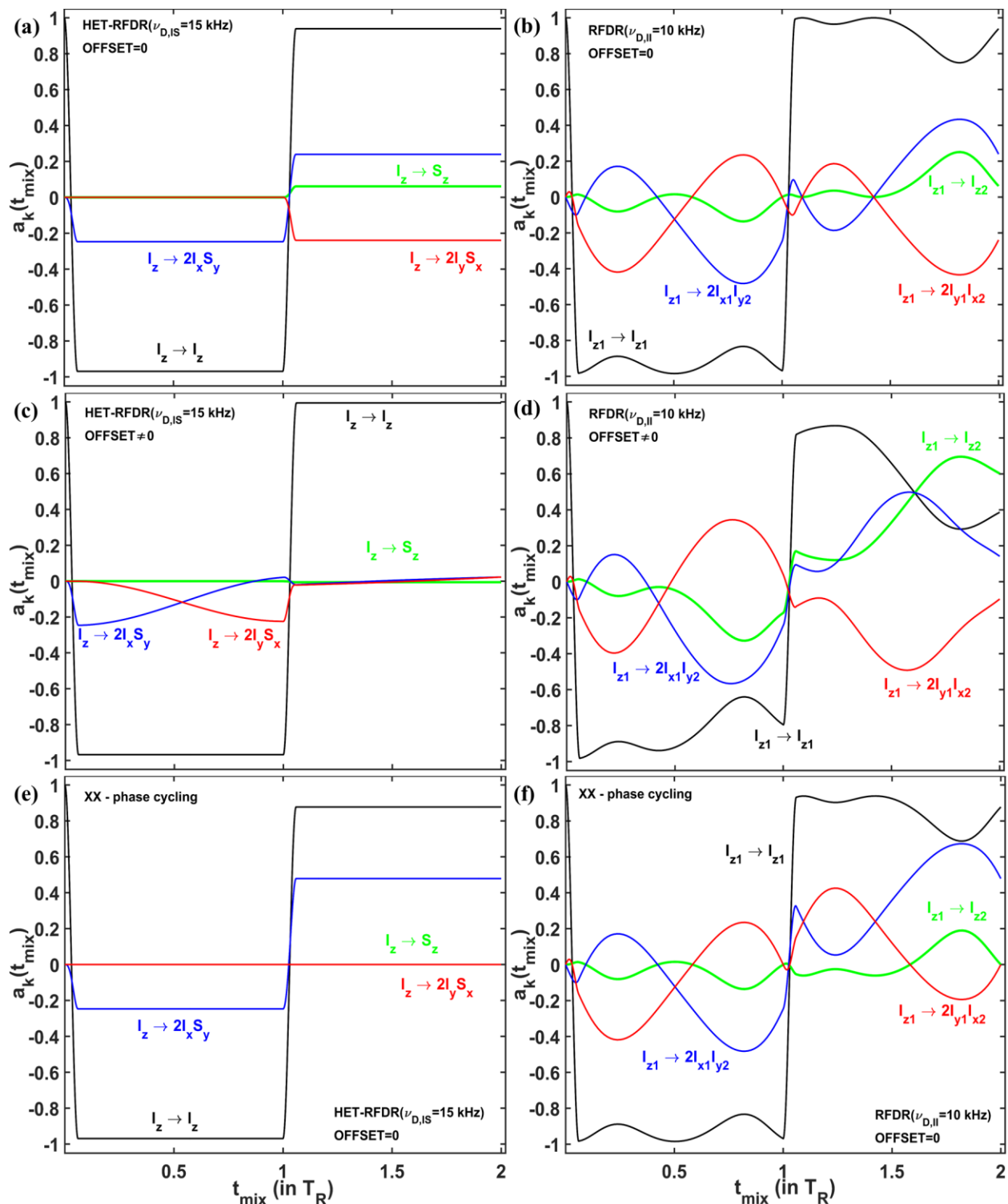
219 In contrast, with a non-zero offset difference, the amplitudes of homonuclear and heteronuclear operators  
 220 do not coincide at any time (Figures 5c and d). Moreover, while the amplitude of  $I_{z1} \rightarrow I_{z2}$  polarization  
 221 transfer is significantly increased (Figure 5d, green line), the corresponding heteronuclear amplitude for  
 222  $I_z \rightarrow S_z$  transfer is significantly decreased (Figure 5c, green line).

223 Figure 5c demonstrates the case, when negligible small HET-RFDR transfer is observed with  $0.5\nu_R$  offset  
 224 difference. To understand the influence of the  $0.5\nu_R$  offset difference for that case, the evolution of the  
 225 operators during first two rotor period is considered. During the first  $\pi_x$  pulse the starting signal is  
 226 transferred from  $I_z$  to  $2I_xS_y$ . Because of the offset difference of  $0.5\nu_R$ , the amplitude of this operator is  
 227 mainly transferred to  $2I_yS_x$  during the first delay (Figure 5c, red line). Since the second  $\pi$ -pulse has phase  
 228  $y$ , there is no transfer from  $2I_yS_x$  to  $I_{z2}$  and very little  $I_z \rightarrow S_z$  polarization transfer overall by the end of  
 229 the second rotor period (Figure 5c, green line).

230 In general, under  $\pm \sim 0.5n\nu_R$  ( $n=1,3,5,\dots$ ) HET-RFDR transfer signal can obtain local minima  
 231 (negative signals, Figure S5 in SI), whereas under  $\pm \sim n\nu_R$  offset difference the local maxima are detected.

232 The demonstrated case in Figure 5c indicates the importance of the phase cycling for RFDR and  
233 HET-RFDR sequences. Figures 5d and f show the evolution of the operators when there is no offset and  
234 both  $\pi$ -pulses have the same phase cycling – XX. For  $IS$  spin system (Figure 5e) only two operators have  
235 nonzero amplitudes during the investigated time:  $I_z$  (black line) and  $2I_xS_y$  (blue line), whereas  $S_z$  and  $2I_yS_x$   
236 are not created. For the  $I_2$  spin system (Figure 5d) all four operators evolve during these two rotor  
237 periods. However, by the end of two rotor periods only two operators have nonzero amplitudes, as for the  
238  $IS$  spin system. In neither case is there magnetization transfer from  $I_z$  to  $S_z$  nor from  $I_{z1}$  to  $I_{z2}$  after one or  
239 two rotor periods. The formal proof of zero transfer signal for homonuclear two spin system in the  
240 absence of offset difference can be found in the SI, “RFDR Phase Cycling” section.

241 Additional spectra and simulation results are found in the supporting information. We recorded proton-  
242 carbon HET-RFDR spectra using fully protonated [ $^{13}\text{C}$ ,  $^{15}\text{N}$ ] labeled SH3. We numerically simulated  
243 multi-spin systems, either containing two protons and two carbons, or one nitrogen and two protons, in  
244 order to track more complex transfer of magnetization. The main conclusions from the simulations and  
245 the experiments in the SI are the agreement between experimental and simulated HET-RFDR transfer  
246 efficiencies, and the expected small dependence of the HET-RFDR recoupling on the flip angle  
247 deviations with XY8 phase cycling (Gullion et al., 1990).



248

249 **Figure 5** The operator evolution through HET-RFDR and RFDR over two rotor periods. The simulated amplitudes of the  
 250 operators of a single crystal (Euler angles:  $184^\circ$ ;  $141^\circ$ ;  $349^\circ$ ) for HET-RFDR ((a), (c)) and RFDR ((b), (d)). For the heteronuclear  
 251  $IS$  spin system, ( $\nu_{D,IS} = 15$  kHz, the initial operator is  $I_z$ ) and for the homonuclear  $I_2$  spin system, ( $\nu_{D,II} = 10$  kHz, the initial

252 operator is  $I_{z1}$ ). The MAS frequency was 10 kHz and the rf-field was 83 kHz. Black lines –  $I_z$  and  $I_{z1}$ ; Green lines –  $S_z$  and  $I_{z2}$ ;  
253 Blue lines –  $2I_xS_y$  and  $2I_{x1}I_{y2}$ ; Red lines –  $2I_yS_x$  and  $2I_{y1}I_{x2}$ . For (a) – (d) the phases of the first and second  $\pi$ -pulses are X and Y,  
254 respectively. (e) and (f) show the case of  $I_S$  and  $I_2$  spin systems, respectively, when the phases of the first and second  $\pi$ -pulses are  
255 both X. (a), (b), (e), (f) – Offset values in kHz: 0, 0. (c) and (d) – Offset values in kHz: 2, -3.

## 256 **Conclusion**

257 In this article we firstly demonstrated HETeronuclear RFDR recoupling, when  $\pi$ -pulses with XY8  
258 phase cycling were applied simultaneously on two channels. Observation of simultaneous heteronuclear  
259 and homonuclear polarization transfers as well as long range contacts were observed in 2D (H)NH spectra  
260 using HET-RFDR for the microcrystalline protein SH3 using  $\alpha$ -PET labeling. The comparison of 1D  
261 HET-RFDR with CP followed by homonuclear RFDR showed similar efficiency of both methods at long  
262 mixing times of about 3ms and longer. We experimentally and numerically demonstrated the dependence  
263 of the HET-RFDR efficiency on the offset difference between dipolar coupled spins. A numerical  
264 operator analysis of both HET-RFDR and RFDR sequences showed that when the offset difference was  
265 small with respect to the MAS frequency, and with measurement at a whole number of rotor periods, the  
266 behavior of HET-RFDR was similar to the well-known homonuclear RFRD. However, different  
267 behaviors were observed when the offset difference could not be neglected.

268 Considering the evolution of a single crystal during HET-RFDR and RFDR, we showed the  
269 operators that were responsible for the transfer. We demonstrated that XY phase cycling of  $\pi$ -pulses has a  
270 crucial role for both HET-RFDR and RFDR transfer. With phase cycling of XX (or  $X\bar{X}$ ) the transfers  
271 between heteronuclear and homonuclear spins did not occur in the absence of offsets. With the presence  
272 of the offset differences when they cannot be neglected in comparison to the MAS rate, RFDR  
273 polarization transfer with phase cycling of XX or  $X\bar{X}$  does occur, although with lower efficiency as was  
274 described before (Bennett et al., 1992).

## 275 **Experimental methods**

276 *Sample preparation:* Microcrystalline chicken alpha spectrin SH3 protein was used for acquisition of all  
277 experimental data. The samples were labeled with 100% protonation at exchangeable sites and either with  
278 alpha proton exchange by transamination ( $\alpha$ -PET) or with uniform  $^{13}\text{C}$  and  $^{15}\text{N}$  labeling with the protocol  
279 described in (Movellan et al., 2019).

280 *Simulations:* HET-RFDR and RFDR simulations were performed with in-house MATLAB scripts using  
281 numerical solution of the equation of motion (Nimerovsky and Goldbourt, 2012).

282 *Solid state NMR spectroscopy:* The HC and (H)N(H)H spectra of  $\alpha$ -PET SH3 were acquired at 14.1 T (600  
283 MHz) using a Bruker AVIIIHD spectrometer using a MASDVT600W2 BL1.3 HXY probe. The  
284 experiments were performed at 10 kHz and 55.555 kHz MAS with the temperature of the cooling gas set  
285 to 280 K and 235 K, respectively.

286 For 1D and 2D  $\alpha$ -PET SH3 (H)N(H)H spectra, the ramped CP transfer from proton to nitrogen was  
287 performed under the same conditions for all experiments: 42.95 kHz on the nitrogen channel and the optimal  
288 ramped amplitude on the proton channel of 86.95-108.69 kHz. The mixing time was 1.05 ms. 9.3 kHz  
289 WALTZ-16 (Shaka et al., 1983) with 25  $\mu\text{s}$  pulses and 10.4 kHz WALTZ-16 (Shaka et al., 1983) with 100  
290  $\mu\text{s}$  pulses were applied on nitrogen and carbon channels during the acquisition. MISSISSIPPI water  
291 suppression (Zhou and Rienstra, 2008) was applied for 100 ms with 13.513 kHz of the rf-field. The carrier  
292 positions were set to 4.6 ppm, 118.5 ppm and 53.7 ppm for  $^1\text{H}$ ,  $^{15}\text{N}$  and  $^{13}\text{C}$ , respectively, except where  
293 otherwise indicated.

294 Table 1 summarizes the applied experimental parameters for 1D spectra.

295 **Table 1** Summary of the experimental parameters used in the 1D CP + RFDR (the start and the end values are shown) and HET-  
296 RFDR using  $\alpha$ -PET labeled SH3.

	CP + RFDR		HET-RFDR
	CP	RFDR	
$^1\text{H}$ (kHz)	86.95-108.69	86.21	86.21
$^{15}\text{N}$ (kHz)	42.95	-	75.75
transfer time (ms)	0.55	[0-7.776]	[0-7.776]

NS	32	32
D1 (s)	2	2
AQ (s)	0.020448	0.020448
SW (kHz)	25	25

297 NS – number of scans; D1 – a recycle delay; AQ – the acquisition time; SW – the spectral width.

298 For 2D (H)N(H)H HET-RFDR spectra, during the indirect dimension 11.6 kHz  $SW_{\text{r-TPPM}}$  (Thakur et al.,  
 299 2006) decoupling with 36.36 us pulses was applied on the proton channel. Two mixing times were used:  
 300 1.152 ms and 3.456 ms. The widths of  $\pi$ -pulses on proton and nitrogen channels were 5.8 us and 6.6 us,  
 301 respectively. 16 scans were acquired per increment in  $t_1$ . The total time for the single 2D experiment was  
 302 10 hours. Table 2 summarizes the rest of the parameters.

303 **Table 2** Summary of the experimental parameters used in 2D HET HET-RFDR  $\alpha$ -PET SH3 experiments.

	AQ1; AQ2 (s)	SW1; SW2 (kHz)	DW1; DW2 (us)
HET-RFDR	0.0527075; 0.020448	9.713; 25	102.94 20

304 1 and 2 are indirect and direct dimensions; AQ – the acquisition time; SW – the spectral width; DW – the dwell time.

305 [2D CP + RFDR experiment with 1.152 and 3.456 ms of mixing time \(only 1D slices are shown in Figure](#)  
 306 [2b\) was performed with the same experimental conditions as 2D HET-RFDR. The CP mixing times from](#)  
 307 [H to N and from N to H were 1.05 ms and 0.55 ms, respectively.](#)

308 For all 1D HC HET-RFDR experiments (Figure 3), 4.8 ms of the mixing time was applied. The widths of  
 309  $\pi$ -pulses on proton and carbon channels were 5.8 us (86.21 kHz) and 6.6 us (75.75 kHz), respectively. 87  
 310 kHz SPINAL64 (Fung et al., 2000) with 6 us pulses was used during the acquisition. 128 scans were  
 311 accumulated. The spectral width was 50 kHz and the acquisition time 0.01536 s.

### 312 Author Contributions

313 EN performed the simulations and discovered HET-RFDR. EN and LBA designed experiments. EN and  
 314 KX recorded data. EN and LBA wrote the article. KTM prepared the SH3 protein samples. All authors  
 315 edited and approved the article.

### 316 Competing Interests



317 The authors declare that they have no conflict of interest.

## 318 **Acknowledgments**

319 We acknowledge financial support from the MPI for Biophysical Chemistry, and from the Deutsche  
320 Forschungsgemeinschaft (Emmy Noether program Grant AN1316/1- 1)

## 321 **References**

322 Andreas, L. B., Le Marchand, T., Jaudzems, K., and Pintacuda, G.: High-resolution proton-detected NMR  
323 of proteins at very fast MAS, *J. Magn. Reson.*, 253, 36–49, <https://doi.org/10.1016/j.jmr.2015.01.003>,  
324 2015.

325 Aucoin, D., Camenares, D., Zhao, X., Jung, J., Sato, T., and Smith, S. O.: High resolution 1H MAS RFDR  
326 NMR of biological membranes, *J. Magn. Reson. San Diego Calif 1997*, 197, 77–86,  
327 <https://doi.org/10.1016/j.jmr.2008.12.009>, 2009.

328 Bak, M., Rasmussen, J. T., and Nielsen, N. C.: SIMPSON : A General Simulation Program for Solid-State  
329 NMR Spectroscopy, *J. Magn. Reson. San Diego Calif 1997*, 1–35,  
330 <https://doi.org/10.1006/jmre.2000.2179>, 2000.

331 Bennett, A. E., Griffin, R. G., Ok, J. H., and Vega, S.: Chemical shift correlation spectroscopy in rotating  
332 solids: Radio frequency-driven dipolar recoupling and longitudinal exchange, *J. Chem. Phys.*, 96, 8624–  
333 8627, <https://doi.org/10.1063/1.462267>, 1992.

334 Bennett, A. E., Rienstra, C. M., Griffiths, J. M., Zhen, W., Lansbury, P. T., and Griffin, R. G.: Homonuclear  
335 radio frequency-driven recoupling in rotating solids, *J. Chem. Phys.*, 108, 9463–9479,  
336 <https://doi.org/10.1063/1.476420>, 1998.

337 Brinkmann, A. and Levitt, M. H.: Symmetry principles in the nuclear magnetic resonance of spinning  
338 solids: Heteronuclear recoupling by generalized Hartmann–Hahn sequences, *J. Chem. Phys.*, 115, 357–  
339 384, <https://doi.org/10.1063/1.1377031>, 2001.

340 Brinkmann, A., Schmedt auf der Günne, J., and Levitt, M. H.: Homonuclear Zero-Quantum Recoupling in  
341 Fast Magic-Angle Spinning Nuclear Magnetic Resonance, *J. Magn. Reson.*, 156, 79–96,  
342 <https://doi.org/10.1006/jmre.2002.2525>, 2002.

343 Carravetta, M., Edén, M., Zhao, X., Brinkmann, A., and Levitt, M. H.: Symmetry principles for the design  
344 of radiofrequency pulse sequences in the nuclear magnetic resonance of rotating solids, *Chem. Phys.*  
345 *Lett.*, 321, 205–215, [https://doi.org/10.1016/S0009-2614\(00\)00340-7](https://doi.org/10.1016/S0009-2614(00)00340-7), 2000.

346 Castellani, F., van Rossum, B., Diehl, A., Schubert, M., Rehbein, K., and Oschkinat, H.: Structure of a  
347 protein determined by solid-state magic-angle-spinning NMR spectroscopy, *Nature*, 420, 99–102,  
348 <https://doi.org/10.1038/nature01070>, 2002.

349 Colvin, M. T., Silvers, R., Frohm, B., Su, Y., Linse, S., and Griffin, R. G.: High Resolution Structural  
350 Characterization of A $\beta$ 42 Amyloid Fibrils by Magic Angle Spinning NMR, *J. Am. Chem. Soc.*, 137, 7509–  
351 7518, <https://doi.org/10.1021/jacs.5b03997>, 2015.

352 Daskalov, A., Martinez, D., Coustou, V., Mammeri, N. E., Berbon, M., Andreas, L. B., Bardiaux, B., Stanek,  
353 J., Noubhani, A., Kauffmann, B., Wall, J. S., Pintacuda, G., Saupe, S. J., Habenstein, B., and Loquet, A.:  
354 Structural and molecular basis of cross-seeding barriers in amyloids, *bioRxiv*, 2020.07.06.188508,  
355 <https://doi.org/10.1101/2020.07.06.188508>, 2020.

356 Ernst, R. R., Bodenhausen, G., and Wokaun, A.: Principles of nuclear magnetic resonance in one and two  
357 dimensions, Oxford Univ. Press, London/New York, 610 pp., 1987.

358 Fritz, M., Kraus, J., Quinn, C. M., Yap, G. P. A., Struppe, J., Sergeyev, I. V., Gronenborn, A. M., and  
359 Polenova, T.: Measurement of Accurate Interfluorine Distances in Crystalline Organic Solids: A High-  
360 Frequency Magic Angle Spinning NMR Approach, *J. Phys. Chem. B*, 123, 10680–10690,  
361 <https://doi.org/10.1021/acs.jpcc.9b08919>, 2019.

362 Fung, B. M., Khitrin, A. K., and Ermolaev, K.: An Improved Broadband Decoupling Sequence for Liquid  
363 Crystals and Solids, *J. Magn. Reson.*, 142, 97–101, <https://doi.org/10.1006/jmre.1999.1896>, 2000.

364 Gelenter, M. D. and Hong, M.: Efficient 15N–13C Polarization Transfer by Third-Spin-Assisted Pulsed  
365 Cross-Polarization Magic-Angle-Spinning NMR for Protein Structure Determination, *J. Phys. Chem. B*,  
366 122, 8367–8379, <https://doi.org/10.1021/acs.jpcc.8b06400>, 2018.

367 Gelenter, M. D., Dregni, A. J., and Hong, M.: Pulsed Third-Spin-Assisted Recoupling NMR for Obtaining  
368 Long-Range 13C–13C and 15N–13C Distance Restraints, *J. Phys. Chem. B*, 124, 7138–7151,  
369 <https://doi.org/10.1021/acs.jpcc.0c04574>, 2020.

370 Grohe, K., Nimerovsky, E., Singh, H., Vasa, S. K., Söldner, B., Voegeli, B., Rienstra, C. M., and Linser, R.:  
371 Exact distance measurements for structure and dynamics in solid proteins by fast-magic-angle-spinning  
372 NMR, *Chem. Commun.*, <https://doi.org/10.1039/C9CC02317H>, 2019.

373 Gullion, T. and Schaefer, J.: Rotational-echo double-resonance NMR, *J. Magn. Reson.* 1969, 81, 196–200,  
374 [https://doi.org/10.1016/0022-2364\(89\)90280-1](https://doi.org/10.1016/0022-2364(89)90280-1), 1989.

375 Gullion, T. and Vega, S.: A simple magic angle spinning NMR experiment for the dephasing of rotational  
376 echoes of dipolar coupled homonuclear spin pairs, *Chem. Phys. Lett.*, 194, 423–428,  
377 [https://doi.org/10.1016/0009-2614\(92\)86076-T](https://doi.org/10.1016/0009-2614(92)86076-T), 1992.

378 Gullion, T., Baker, D. B., and Conradi, M. S.: New, compensated Carr-Purcell sequences, *J. Magn. Reson.*  
379 1969, 89, 479–484, [https://doi.org/10.1016/0022-2364\(90\)90331-3](https://doi.org/10.1016/0022-2364(90)90331-3), 1990.

380 Haeberlen, U. and Waugh, J. S.: Coherent Averaging Effect in Magnetic Resonance, *Phys. Rev.*, 175, 453–  
381 467, <https://doi.org/10.1103/PhysRev.175.453>, 1968.

382 Hartmann, S. R. and Hahn, E. L.: Nuclear Double Resonance in the Rotating Frame, *Phys. Rev.*, 128,  
383 2042–2053, <https://doi.org/10.1103/PhysRev.128.2042>, 1962.

384 Hediger, S., Meier, B. H., Kurur, N. D., Bodenhausen, G., and Ernst, R. R.: NMR cross polarization by  
385 adiabatic passage through the Hartmann—Hahn condition (APHH), *Chem. Phys. Lett.*, 223, 283–288,  
386 [https://doi.org/10.1016/0009-2614\(94\)00470-6](https://doi.org/10.1016/0009-2614(94)00470-6), 1994.

387 Hellwagner, J., Wili, N., Ibáñez, L. F., Wittmann, J. J., Meier, B. H., and Ernst, M.: Transient effects in  $\pi$ -  
388 pulse sequences in MAS solid-state NMR, *J. Magn. Reson.*, 287, 65–73,  
389 <https://doi.org/10.1016/j.jmr.2017.12.015>, 2018.

390 Hing, A. W., Vega, S., and Schaefer, J.: Transferred-echo double-resonance NMR, *J. Magn. Reson.* 1969,  
391 96, 205–209, [https://doi.org/10.1016/0022-2364\(92\)90305-Q](https://doi.org/10.1016/0022-2364(92)90305-Q), 1992.

392 Hou, G., Byeon, I.-J. L., Ahn, J., Gronenborn, A. M., and Polenova, T.:  $1\text{H}$ – $^{13}\text{C}/1\text{H}$ – $^{15}\text{N}$  Heteronuclear  
393 Dipolar Recoupling by R-Symmetry Sequences Under Fast Magic Angle Spinning for Dynamics Analysis of  
394 Biological and Organic Solids, *J. Am. Chem. Soc.*, 133, 18646–18655, <https://doi.org/10.1021/ja203771a>,  
395 2011a.

396 Hou, G., Yan, S., Sun, S., Han, Y., Byeon, I.-J. L., Ahn, J., Concel, J., Samoson, A., Gronenborn, A. M., and  
397 Polenova, T.: Spin Diffusion Driven by R-Symmetry Sequences: Applications to Homonuclear Correlation  
398 Spectroscopy in MAS NMR of Biological and Organic Solids, *J. Am. Chem. Soc.*, 133, 3943–3953,  
399 <https://doi.org/10.1021/ja108650x>, 2011b.

400 Hou, G., Yan, S., Trébosc, J., Amoureux, J.-P., and Polenova, T.: Broadband homonuclear correlation  
401 spectroscopy driven by combined R2nv sequences under fast magic angle spinning for NMR structural  
402 analysis of organic and biological solids, *J. Magn. Reson.*, 232, 18–30,  
403 <https://doi.org/10.1016/j.jmr.2013.04.009>, 2013.

404 Ishii, Y.:  $^{13}\text{C}$ – $^{13}\text{C}$  dipolar recoupling under very fast magic angle spinning in solid-state nuclear magnetic  
405 resonance: Applications to distance measurements, spectral assignments, and high-throughput  
406 secondary-structure determination, *J. Chem. Phys.*, 114, 8473–8483,  
407 <https://doi.org/10.1063/1.1359445>, 2001.

408 Jain, M. G., Lalli, D., Stanek, J., Gowda, C., Prakash, S., Schwarzer, T. S., Schubeis, T., Castiglione, K.,  
409 Andreas, L. B., Madhu, P. K., Pintacuda, G., and Agarwal, V.: Selective  $1\text{H}$ – $1\text{H}$  Distance Restraints in Fully  
410 Protonated Proteins by Very Fast Magic-Angle Spinning Solid-State NMR, *J. Phys. Chem. Lett.*, 8, 2399–  
411 2405, <https://doi.org/10.1021/acs.jpcclett.7b00983>, 2017.

412 Jaroniec, C. P., Filip, C., and Griffin, R. G.: 3D TEDOR NMR Experiments for the Simultaneous  
413 Measurement of Multiple Carbon–Nitrogen Distances in Uniformly  $^{13}\text{C},^{15}\text{N}$ -Labeled Solids, *J. Am.*  
414 *Chem. Soc.*, 124, 10728–10742, <https://doi.org/10.1021/ja026385y>, 2002.

415 Ji, Y., Liang, L., Guo, C., Bao, X., Polenova, T., and Hou, G.: Zero-Quantum Homonuclear Recoupling  
416 Symmetry Sequences in Solid-State Fast MAS NMR Spectroscopy, *Acta Phys.-Chim. Sin.*, 36, 1905029–  
417 1905034, 2020.

418 Linser, R., Bardiaux, B., Andreas, L. B., Hyberts, S. G., Morris, V. K., Pintacuda, G., Sunde, M., Kwan, A. H.,  
419 and Wagner, G.: Solid-State NMR Structure Determination from Diagonal-Compensated, Sparsely  
420 Nonuniform-Sampled 4D Proton–Proton Restraints, *J. Am. Chem. Soc.*, 136, 11002–11010,  
421 <https://doi.org/10.1021/ja504603g>, 2014.

- 422 Maricq, M. M.: Application of average hamiltonian theory to the NMR of solids, *Phys. Rev. B*, 25, 6622–  
423 6632, <https://doi.org/10.1103/PhysRevB.25.6622>, 1982.
- 424 Mehring, M.: Principles of High Resolution NMR in Solids, 2nd ed., Springer-Verlag, Berlin Heidelberg,  
425 <https://doi.org/10.1007/978-3-642-68756-3>, 1983.
- 426 Meier, B. H. and Earl, W. L.: Excitation of multiple quantum transitions under magic angle spinning  
427 conditions: Adamantane, *J. Chem. Phys.*, 85, 4905–4911, <https://doi.org/10.1063/1.451726>, 1986.
- 428 Messinger, R. J., Ménétrier, M., Salager, E., Boulineau, A., Duttine, M., Carlier, D., Ateba Mba, J.-M.,  
429 Croguennec, L., Masquelier, C., Massiot, D., and Deschamps, M.: Revealing Defects in Crystalline  
430 Lithium-Ion Battery Electrodes by Solid-State NMR: Applications to LiVPO<sub>4</sub>F, *Chem. Mater.*, 27, 5212–  
431 5221, <https://doi.org/10.1021/acs.chemmater.5b01234>, 2015.
- 432 Metz, G., Wu, X. L., and Smith, S. O.: Ramped-Amplitude Cross Polarization in Magic-Angle-Spinning  
433 NMR, *J. Magn. Reson. A*, 110, 219–227, <https://doi.org/10.1006/jmra.1994.1208>, 1994.
- 434 Movellan, K. T., Najbauer, E. E., Pratihari, S., Salvi, M., Giller, K., Becker, S., and Andreas, L. B.: Alpha  
435 protons as NMR probes in deuterated proteins, *J. Biomol. NMR*, 73, 81–91,  
436 <https://doi.org/10.1007/s10858-019-00230-y>, 2019.
- 437 Nielsen, N. Chr., Strassø, L. A., and Nielsen, A. B.: Dipolar Recoupling, in: *Solid State NMR*, edited by:  
438 Chan, J. C. C., Springer, Berlin, Heidelberg, 1–45, [https://doi.org/10.1007/128\\_2011\\_129](https://doi.org/10.1007/128_2011_129), 2012.
- 439 Nimerovsky, E. and Goldbourt, A.: Insights into the spin dynamics of a large anisotropy spin subjected to  
440 long-pulse irradiation under a modified REDOR experiment., *J. Magn. Reson.*, 225, 130–41,  
441 <https://doi.org/10.1016/j.jmr.2012.09.015>, 2012.
- 442 Nishiyama, Y., Malon, M., Ishii, Y., and Ramamoorthy, A.: 3D <sup>15</sup>N/<sup>15</sup>N/<sup>1</sup>H chemical shift correlation  
443 experiment utilizing an RFDR-based <sup>1</sup>H/<sup>1</sup>H mixing period at 100kHz MAS, *J. Magn. Reson.*, 244, 1–5,  
444 <https://doi.org/10.1016/j.jmr.2014.04.008>, 2014a.
- 445 Nishiyama, Y., Zhang, R., and Ramamoorthy, A.: Finite-pulse radio frequency driven recoupling with  
446 phase cycling for 2D <sup>1</sup>H/<sup>1</sup>H correlation at ultrafast MAS frequencies, *J. Magn. Reson.*, 243, 25–32,  
447 <https://doi.org/10.1016/j.jmr.2014.03.004>, 2014b.
- 448 Ok, J. H., Spencer, R. G. S., Bennett, A. E., and Griffin, R. G.: Homonuclear correlation spectroscopy in  
449 rotating solids, *Chem. Phys. Lett.*, 197, 389–395, [https://doi.org/10.1016/0009-2614\(92\)85790-H](https://doi.org/10.1016/0009-2614(92)85790-H), 1992.
- 450 Olejniczak, E. T., Vega, S., and Griffin, R. G.: Multiple pulse NMR in rotating solids, *J. Chem. Phys.*, 81,  
451 4804–4817, <https://doi.org/10.1063/1.447506>, 1984.
- 452 Pandey, M. K. and Nishiyama, Y.: A one-dimensional solid-state NMR approach for <sup>14</sup>NH/<sup>14</sup>NH overtone  
453 correlation through <sup>1</sup>H/<sup>1</sup>H mixing under fast MAS, *Phys. Chem. Chem. Phys.*, 20, 25849–25853,  
454 <https://doi.org/10.1039/C8CP05000G>, 2018.
- 455 Pandey, M. K., Vivekanandan, S., Yamamoto, K., Im, S., Waskell, L., and Ramamoorthy, A.: Proton-  
456 detected 2D radio frequency driven recoupling solid-state NMR studies on micelle-associated  
457 cytochrome-b5, *J. Magn. Reson.*, 242, 169–179, <https://doi.org/10.1016/j.jmr.2014.02.016>, 2014.

458 Petkova, A. T., Ishii, Y., Balbach, J. J., Antzutkin, O. N., Leapman, R. D., Delaglio, F., and Tycko, R.: A  
459 structural model for Alzheimer's -amyloid fibrils based on experimental constraints from solid state  
460 NMR, *Proc. Natl. Acad. Sci.*, 99, 16742–16747, <https://doi.org/10.1073/pnas.262663499>, 2002.

461 Roos, M., Mandala, V. S., and Hong, M.: Determination of Long-Range Distances by Fast Magic-Angle-  
462 Spinning Radiofrequency-Driven 19F–19F Dipolar Recoupling NMR, *J. Phys. Chem. B*, 122, 9302–9313,  
463 <https://doi.org/10.1021/acs.jpcc.8b06878>, 2018.

464 Rovnyak, D.: Tutorial on analytic theory for cross-polarization in solid state NMR, *Concepts Magn. Reson.*  
465 Part A, 32A, 254–276, <https://doi.org/10.1002/cmr.a.20115>, 2008.

466 Saalwächter, K.: Robust NMR Approaches for the Determination of Homonuclear Dipole–Dipole  
467 Coupling Constants in Studies of Solid Materials and Biomolecules, *ChemPhysChem*, 14, 3000–3014,  
468 <https://doi.org/10.1002/cphc.201300254>, 2013.

469 Shaka, A. J., Keeler, J., Frenkiel, T., and Freeman, R.: An improved sequence for broadband decoupling:  
470 WALTZ-16, *J. Magn. Reson.* 1969, 52, 335–338, [https://doi.org/10.1016/0022-2364\(83\)90207-X](https://doi.org/10.1016/0022-2364(83)90207-X), 1983.

471 Shen, M., Hu, B., Lafon, O., Trébosc, J., Chen, Q., and Amoureux, J.-P.: Broadband finite-pulse radio-  
472 frequency-driven recoupling (fp-RFDR) with (XY8)<sub>41</sub> super-cycling for homo-nuclear correlations in very  
473 high magnetic fields at fast and ultra-fast MAS frequencies, *J. Magn. Reson.*, 223, 107–119,  
474 <https://doi.org/10.1016/j.jmr.2012.07.013>, 2012.

475 Shi, C., Fricke, P., Lin, L., Chevelkov, V., Wegstroth, M., Giller, K., Becker, S., Thanbichler, M., and Lange,  
476 A.: Atomic-resolution structure of cytoskeletal bactofilin by solid-state NMR, *Sci. Adv.*, 1,  
477 <https://doi.org/10.1126/sciadv.1501087>, 2015.

478 Slichter, C. P.: *Principles of Magnetic Resonance*, 3rd ed., Springer-Verlag, Berlin Heidelberg,  
479 <https://doi.org/10.1007/978-3-662-09441-9>, 1990.

480 Sun, B. Q., Costa, P. R., and Griffin, R. G.: Heteronuclear Polarization Transfer by Radiofrequency-Driven  
481 Dipolar Recoupling Under Magic-Angle Spinning, *J. Magn. Reson. A*, 112, 191–198,  
482 <https://doi.org/10.1006/jmra.1995.1031>, 1995.

483 Szeverenyi, N. M., Sullivan, M. J., and Maciel, G. E.: Observation of spin exchange by two-dimensional  
484 fourier transform <sup>13</sup>C cross polarization-magic-angle spinning, *J. Magn. Reson.* 1969, 47, 462–475,  
485 [https://doi.org/10.1016/0022-2364\(82\)90213-X](https://doi.org/10.1016/0022-2364(82)90213-X), 1982.

486 Takegoshi, K., Nakamura, S., and Terao, T.: <sup>13</sup>C–<sup>1</sup>H dipolar-assisted rotational resonance in magic-angle  
487 spinning NMR, *Chem. Phys. Lett.*, 344, 631–637, [https://doi.org/10.1016/S0009-2614\(01\)00791-6](https://doi.org/10.1016/S0009-2614(01)00791-6), 2001.

488 Tang, M., Berthold, D. A., and Rienstra, C. M.: Solid-State NMR of a Large Membrane Protein by  
489 Paramagnetic Relaxation Enhancement, *J. Phys. Chem. Lett.*, 2, 1836–1841,  
490 <https://doi.org/10.1021/jz200768r>, 2011.

491 Thakur, R. S., Kurur, N. D., and Madhu, P. K.: Swept-frequency two-pulse phase modulation for  
492 heteronuclear dipolar decoupling in solid-state NMR, *Chem. Phys. Lett.*, 426, 459–463,  
493 <https://doi.org/10.1016/j.cplett.2006.06.007>, 2006.

494 Tycko, R. and Dabbagh, G.: Measurement of nuclear magnetic dipole—dipole couplings in magic angle  
495 spinning NMR, *Chem. Phys. Lett.*, 173, 461–465, [https://doi.org/10.1016/0009-2614\(90\)87235-J](https://doi.org/10.1016/0009-2614(90)87235-J), 1990.

496 Wong, K. M., Wang, Y., Seroski, D. T., Larkin, G. E., Mehta, A. K., Hudalla, G. A., Hall, C. K., and Paravastu,  
497 A. K.: Molecular complementarity and structural heterogeneity within co-assembled peptide  $\beta$ -sheet  
498 nanofibers, *Nanoscale*, 12, 4506–4518, <https://doi.org/10.1039/C9NR08725G>, 2020.

499 Wu, X. L. and Zilm, K. W.: Cross Polarization with High-Speed Magic-Angle Spinning, *J. Magn. Reson. A*,  
500 104, 154–165, <https://doi.org/10.1006/jmra.1993.1203>, 1993.

501 Zhang, R., Nishiyama, Y., Sun, P., and Ramamoorthy, A.: Phase cycling schemes for finite-pulse-RFDR  
502 MAS solid state NMR experiments, *J. Magn. Reson.*, 252, 55–66,  
503 <https://doi.org/10.1016/j.jmr.2014.12.010>, 2015.

504 Zhang, R., Mroue, K. H., and Ramamoorthy, A.: Proton-Based Ultrafast Magic Angle Spinning Solid-State  
505 NMR Spectroscopy, *Acc. Chem. Res.*, 50, 1105–1113, <https://doi.org/10.1021/acs.accounts.7b00082>,  
506 2017.

507 Zhang, Z., Chen, Y., and Yang, J.: Band-selective heteronuclear dipolar recoupling with dual back-to-back  
508 pulses in rotating solids, *J. Magn. Reson.*, 272, 46–52, <https://doi.org/10.1016/j.jmr.2016.09.003>, 2016.

509 Zhang, Z., Oss, A., Org, M.-L., Samoson, A., Li, M., Tan, H., Su, Y., and Yang, J.: Selectively Enhanced  $1\text{H}$ –  
510  $1\text{H}$  Correlations in Proton-Detected Solid-State NMR under Ultrafast MAS Conditions, *J. Phys. Chem.*  
511 *Lett.*, 11, 8077–8083, <https://doi.org/10.1021/acs.jpcclett.0c02412>, 2020.

512 Zheng, Z., Qiang, W., and Weliky, D. P.: Investigation of finite-pulse radiofrequency-driven recoupling  
513 methods for measurement of intercarbonyl distances in polycrystalline and membrane-associated HIV  
514 fusion peptide samples, *Magn. Reson. Chem.*, 45, S247–S260, <https://doi.org/10.1002/mrc.2160>, 2007.

515 Zhou, D. H. and Rienstra, C. M.: High-performance solvent suppression for proton detected solid-state  
516 NMR, *J. Magn. Reson.*, 192, 167–172, <https://doi.org/10.1016/j.jmr.2008.01.012>, 2008.

517 Zhou, D. H., Nieuwkoop, A. J., Berthold, D. A., Comellas, G., Sperling, L. J., Tang, M., Shah, G. J., Brea, E.  
518 J., Lemkau, L. R., and Rienstra, C. M.: Solid-state NMR analysis of membrane proteins and protein  
519 aggregates by proton detected spectroscopy, *J. Biomol. NMR*, 54, 291–305,  
520 <https://doi.org/10.1007/s10858-012-9672-z>, 2012.

521 Zinke, M., Fricke, P., Lange, S., Zinn-Justin, S., and Lange, A.: Protein–Protein Interfaces Probed by  
522 Methyl Labeling and Proton-Detected Solid-State NMR Spectroscopy, *Chemphyschem*, 19, 2457–2460,  
523 <https://doi.org/10.1002/cphc.201800542>, 2018.

524

525